Carbohydrate Polymers 342 (2024) 122390

Contents lists available at ScienceDirect

Carbohydrate Polymers

journal homepage: www.elsevier.com/locate/carbpol

Controlled shrinkage of cellulose nanofibril films to enhance mechanical and barrier properties

Md Ikramul Hasan [a,c], Jinwu Wang [a,b,c], Mehdi Tajvidi [a,c,*]

[a] School of Forest Resources, University of Maine, 5755 Nutting Hall, Orono, ME 04469, USA
[b] Forest Products Laboratory, U.S. Forest Service, 1 Gifford Pinchot Drive, Madison, WI 53726, USA
[c] Advanced Structures and Composites Center, University of Maine, 35 Flagstaff Road, Orono, ME 04469, USA

ARTICLE INFO

Keywords:
Cellulose nanofibrils
Shrinkage
Drying
Packaging
Gas barrier

ABSTRACT

Standalone cellulose nanofibril (CNF) films have a natural tendency to shrink upon drying from wet conditions due to capillary drying stresses. This shrinkage happens in both the radial direction, and the vertical direction. In this study, we prepared two types of CNF films- one in a restrained condition that did not allow shrinkage in the radial direction but enabled it in the vertical direction and another with 11 % radial shrinkage but limited vertical shrinkage. The radial shrinkage led to a more porous structure than the vertical shrinkage, which brought about poorer oxygen/moisture barrier performance. However, the density and oxygen permeability of the films converged to a similar value upon a simple thermocompression process. Radial shrinkage resulted in 140 % and 90 % higher strain at break and toughness in films with a significant sacrifice in strength and modulus. Scanning electron microscopy revealed that radial shrinkage formed wavy layers in the core structure leaving more free space, whereas vertical shrinkage formed flatter layers. Radial shrinkage is likely to produce a thicker individual layer in the core structure of CNF films than vertical shrinkage. The insight from this study will help tune the mechanical and barrier performance of CNF films and their composites.

1. Introduction

Food packaging, advanced electronics, and optics rely heavily on polymeric films with excellent gas barriers and mechanical performance, yet many of these films have performance limitations for the desired application or pose serious environmental and sustainability concerns (Barlow & Morgan, 2013; Gao et al., 2019; Paquet & Kumacheva, 2008). A viable biobased substitute for petroleum-based polymeric films is cellulose nanofibril (CNF) film. CNFs, a mechanically defibrillated form of wood pulp with a high aspect ratio (4–20 nm wide and 0.5–2 μm long) (Moon et al., 2011) have gained increased attention for developing high-strength films (Yang et al., 2020), as a filler in a polymeric matrix (Abdul Khalil et al., 2012), as a binder for wood particles and natural fibers (Tayeb et al., 2018), and high gas barrier applications in food packaging (Wang et al., 2018).

The pristine CNF films are typically formed from their liquid hydrocolloids through the evaporation of water. The film of CNFs can be formed by a simple casting method that allows drying of the film at room temperature, which eventually takes a considerable amount of time. However, a more scalable approach for CNF film making is a vacuum filtration process that first forms a wet mat through a significant reduction in water content. Ultimately, this wet mat needs to be dried in the air or at elevated temperatures in an oven or hot-press (Hasan et al., 2021). Therefore, drying is a key step to control the final cost and properties of CNF films. However, cellulose-containing materials (including wood) are considered compressible multiscale porous materials as they are susceptible to fracture or shrinkage during drying in unrestrained conditions due to capillary drying stresses (Lerouge et al., 2020). As a result, the drying-induced shrinkage of CNF films has been reported in numerous research studies (Fein et al., 2021; Sim et al., 2015). Where shrinkage is undesirable, such as in the production of foams and aerogels, special drying procedures including freeze-drying, supercritical drying, and microwave-assisted drying are applied to avoid shrinkage (Chen et al., 2021; Hafez & Tajvidi, 2021).

Understanding different processes and characteristics involved in drying CNF films including shrinkage from a wet mat is crucial to understanding the final dry film properties. Qing et al. (2015) were the first to report changes in the structure and mechanical properties of dry films produced by air, oven, and freeze-drying techniques (Qing et al., 2015). As a supplement to this work, our group conducted a detailed analysis of

* Corresponding author at: School of Forest Resources, University of Maine, 5755 Nutting Hall, Orono, ME 04469, USA.
E-mail addresses: md.hasan@maine.edu (M.I. Hasan), jinwu.wang@usda.gov (J. Wang), mehdi.tajvidi@maine.edu (M. Tajvidi).

https://doi.org/10.1016/j.carbpol.2024.122390
Received 4 April 2024; Received in revised form 25 May 2024; Accepted 8 June 2024
Available online 11 June 2024
0144-8617/© 2024 Elsevier Ltd. All rights are reserved, including those for text and data mining, AI training, and similar technologies.

the mechanical as well as barrier performance of refiner-produced CNF films induced by air, oven, heat-gun, and hot-press drying (Hasan et al., 2021). Ghasemi et al. (2020) showed that the orientation of the CNF films can be influenced by stretching and controlled drying (restrained and unrestrained drying) and developed a polarized light microscope-based method to quantify the orientation of fibrils in CNF films (Ghasemi et al., 2020). Fein et al. (2021) provided a comprehensive investigation of the impacts of casting and filtration techniques on the final mechanical and water vapor barrier properties of the films and illustrated a skin-core model for the formation of CNF films from wet suspension (Fein et al., 2021). To the best of our knowledge, however, there is no detailed investigation on the influence of shrinkage on the mechanical and gas barrier properties of refiner-produced CNF films.

Understanding the relationship between shrinkage and the ultimate properties of CNF films can be critical. For example, tensile strain at break values of films made from the same refiner-produced neat CNF films varied from 2 % to 20 % in the literature (Amini et al., 2020; El Awad Azrak et al., 2019; Fein et al., 2021; Ghasemi et al., 2020). This significant variation across films made from the same material may be explained by the variation in testing parameters and film dimensions, as well as the variation in the shrinkage caused by the different film preparation techniques. Ghasemi et al. (2020) highlighted in their research a potential change in the strain at break difference due to shrinkage (Ghasemi et al., 2020). Shrinkage is anticipated for cast CNF films as the suspension dries without any pressure or constraint that can interfere with the natural tendency of CNFs to shrink. For the filtered wet mat, researchers prefer restrained drying to prevent the curling of films upon drying, which would complicate further testing of the films' different properties. However, the prevention of shrinkage may be responsible for the loss of some desired properties for the target application, which is yet to be explored for neat CNF films. At the minimum, based on some shrinkage studies conducted on the wet paper mat on an industrial and laboratory scale, it is obvious that shrinkage offers substantially greater extensibility in dry paper/paperboard (Ketola et al., 2019; Kouko & Retulainen, 2018). Even industries employ special processes like Clupak and Expanda to improve in-plane compaction and creping coupled with shrinkage for the manufacturing of high extensibility papers (Wu et al., 2022). However, none of the studies on wet paper mats linked shrinkage to barrier performance as paper is not expected to have good gas barrier properties anyway, which is not true for CNF films.

Based on the above discussion, we hypothesize that the shrinkage of CNF films during drying process is one of the major factors that can significantly influence physical, mechanical and barrier properties of CNF films, which is often overlooked by researchers when reporting the properties of CNF films. To test this hypothesis, we divided the shrinkage into two distinct directions, the shrinkage in the radial direction (referred to as 'xy-shrinkage' and measured by the percentage change in the diameter of circular films) and the shrinkage in the vertical direction (referred to as 'z-shrinkage' and measured by the percentage change in thickness), to clearly understand the contribution of each component instead of traditional volumetric shrinkage-based measurement. We designed a simple experimental technique to keep all process parameters for film preparation the same, except the condition of drying (restrained vs unrestrained) to understand the effect of shrinkage. We prepared two sets of films, one with a greater xy-shrinkage (referred to as 'xy' film) and one with no xy-shrinkage (referred to as 'z' film). However, both films, including the one referred to as xy film, experienced z-shrinkage, i.e., thickness reduction, albeit the relative amount of z-shrinkage varied. Inspired by our previous work, we were also motivated to quantify the influence of thermo-compression on dry xy and z films and referred to them as 'xy-z' and 'z-z', respectively. Finally, an illustrative structural understanding of the film's surface, core structure, and single layer formation induced by the shrinkage was demonstrated and linked to the mechanical and barrier properties, which can have a significant impact on future efforts to explain refiner-produced CNF films' behavior.

2. Materials and methods

2.1. Materials

CNFs in the form of 3 wt% (solid content) slurry were kindly provided by the Process Development Center, University of Maine. They were produced from northern softwood kraft pulp using a low-energy demanding refiner following a patented technique (Bilodeau & Paradis, 2018). The final fines content of these CNFs was 90 %, i.e., 90 % of fibrils had a length of <200 μm. The mean diameter of these fibrils obtained from TEM was 37 nm and the mean roughness measured by AFM was 133 nm. A detailed morphological analysis of the same fibrils was described (referred to as 'standard CNFs') in our previous work (Hasan et al., 2021).

2.2. Film preparation

CNF films were produced through a vacuum filtration method. A schematic diagram of the film preparation process is shown in Fig. 1a. The CNF suspension was first diluted to 0.5 wt% by adding distilled water. The suspension was then sonicated for 2 min using a Branson 450 Sonifier (Ultrasonics Corporation, CT, USA) at 20 % output power. For the filtration setup, a ceramic Buchner funnel with an internal diameter of 11 cm was placed on a conical flask and coupled to a suction pump that maintained a 254 mm (Hg) suction pressure. A Whatman Grade 5 (2.5 μm pore size) was used as the membrane for filtration and the filtration was continued until the interval between two consecutive droplets exiting the funnel was 20 s. The wet film with the filter paper was then extracted from the funnel and placed on a blotting paper to absorb excess water.

Before drying, the wet film was cold-pressed using a Dake (MI, USA) hydraulic press to reduce the water content to ~50 %. During the cold press, a new filter paper (the old one was still on the bottom side of the film) was placed on top of the wet film, which was then sandwiched between two blotting papers and two circular steel plates. Following cold pressing, the blotting papers were removed. Now, depending on the type of shrinkage desired, we either left the filter papers on both surfaces (z-shrinkage) or eliminated both filter papers (xy-shrinkage) from the wet film. The circular steel plates were retained on both sides of the cold-pressed films for drying. This time, however, a ring-shaped spacer made by layering aluminum foil was placed between the two steel plates to ensure that the shrinkage was not restrained by the pressure.

We utilized a hot press (Carver Inc., Wabash, IN) at 150 °C for 8 min for drying. However, we did not employ any pressure (pressure reading zero) during drying, rather the hot platens were just in contact with the two steel plates to prevent the curling and warping of the films after drying. The films that were dried without filter papers ('xy' film) shrank in the radial direction, whereas the films dried on filter papers ('z' film) did not show any radial shrinkage. It is important to point out that both xy and z films had vertical shrinkage, albeit the degree of vertical shrinkage was different for the two films as will be addressed in Section 3.1. Both samples were then hot-pressed for a second time after drying without any filter paper at an elevated pressure (1.1 MPa) for 4 min to generate two more sets of samples ('xy-z' and 'z-z'). Before any measurements were made, these four sets of samples were conditioned for at least 24 h at 23 °C and 50 % relative humidity.

2.3. Physical and surface properties

2.3.1. Density

A 9 cm circle was cut from each conditioned film using a circle cutter and the weight was measured using a balance (0.0001 g accuracy). The thickness of each sample was determined by averaging the thickness of 10 points around a single film using a micrometer (0.001 mm accuracy). Then the density was measured by dividing the conditioned weight of the film by the corresponding volume calculated from the radius and

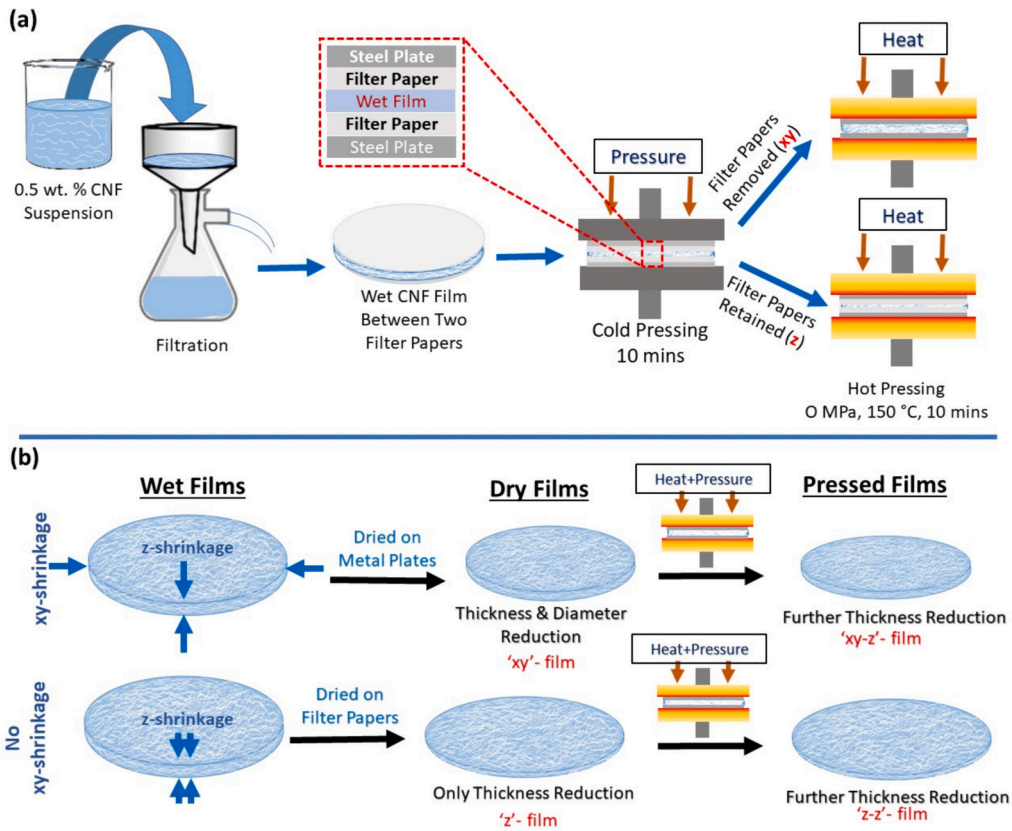

Fig. 1. A schematic diagram of the film preparation process for xy and z films (a) and corresponding volume reduction mechanism from wet films to dry films and pressed films (b).

average thickness. Five density measurements were taken for each shrinkage type to obtain the mean density value. The porosity of each film was calculated depending on the film density (ρ_f) and pure cellulose density ($\rho_c = 1.5$ g/cm^3) from Eq. (1).

$$Porosity\ (\%) = \frac{\rho_c - \rho_f}{\rho_c} \times 100\% \quad (1)$$

2.3.2. Transmittance

A UV–Vis spectrophotometer (Lambda 365+, PerkinElmer, MA, USA) was used to measure the visible light transmittance (400–800 nm) of the films. The spectrophotometer had an internal sample holder designed for film transmittance and air was used as a reference.

2.4. Oxygen and water vapor permeability

2.4.1. Oxygen permeability

The oxygen transmission rate (OTR) of the films was measured at 23 °C and 80 % relative humidity following ASTM D3985-17 standard. Before testing, all films were conditioned at 80 % relative humidity for at least 24 h in a conditioning chamber and then inside the testing machine for 6 h. A Mocon Ox-Tran 2/22 OTR analyzer was used to measure the OTR. After conditioning, the machine went through a 'rezero' process that cleaned the sensor and film purging 98 % N_2 and 2 % H_2 for 15 min and then recorded the OTR value after 15 min of 100 % oxygen transmission through the film. The machine ran the rezero process after every two tests and continued the same testing cycle until the difference between the last five OTR values converged to <1 % difference. The OTR values of each film were normalized by thickness to obtain the oxygen permeability (OP) value.

2.4.2. Water vapor permeability

A gravimetric method following a slightly modified form of ASTM E96/E96M-16 was used to measure the water vapor transmission rate (WVTR). Each film was trimmed into 65 mm (radius, r = 32.5 mm) circles and affixed on top of a Mason jar (Rubbermaid Incorporated, GA, USA) using a metal screw cap and sealed with silicone rubber. Before placing the film, the jar was filled up with 60 g of distilled water. The entire jar was then left in an environmental chamber of 23 °C and 50 % relative humidity. After conditioning for 48 h, the weight loss (Δ_{mass}) of the Mason jar was recorded over 24 h time difference. The WVTR was then calculated from Eq. (2).

$$\text{WVTR}\left(\frac{g}{m^2.day}\right) = \frac{\Delta_{mass}}{\Pi r^2.day} \quad (2)$$

The WVTR was then thickness and pressure normalized using Eq. (3) to obtain water vapor permeability. The quantity $P_{(saturated)}$ and $\Delta_{RH\%}$ in Eq. (3), respectively, indicated the saturated vapor pressure of water at 23 °C (2.81 kPa) and the difference in relative humidity between the inside (100 %) and outside (50 %) of the jar.

$$\text{WVP}\left(\frac{g.mm}{m^2.day.kPa}\right) = \text{WVTR} \times \frac{Thickness \times 100}{P_{saturated} \times \Delta_{RH\%}} \quad (3)$$

2.5. Microscopic analysis

2.5.1. Optical microscope

A polarized light microscope (AmScope™, ME520TA, Irvine, CA) was used to track the fibrils during drying on two different substrates. The first substrate was a regular microscopic glass slide, which can be considered as an interacting surface for CNF suspension based on the surface free energy whereas the other one was a plastic film substrate taped on the microscopic glass slide. The plastic film was cut from the

MINIGRIP® Red Line™ Reclosable bags that acted as a non-interacting surface for CNF suspension based on surface free energy. A detailed discussion on choosing those substrates is provided in Section 3.4. A 0.01 wt% suspension of CNFs was prepared and then a small volume (~0.05 mL) was drop-casted on both substrates. Images and video were recorded at 50× magnification for analysis. Besides the optical microscope, an HDMI microscope camera (ShenZhen Hayear Electronics, China) with a mounted lens was used to capture the images of the full droplet drying.

2.5.2. Scanning electron microscope

Micron-scale images of film surfaces and cross-sections were captured at different magnifications using a Zeiss Nvision 40 (Zeiss, Germany) Focused Ion Beam (FIB) Scanning Electron Microscope (SEM). For cross-section analysis, the films were first freeze-fractured using liquid nitrogen. Then all the pieces of the films including the ones for surface analysis were sputter-coated with a 4 nm layer of Au/Pd to avoid charge accumulation on the surfaces. The voltage was kept at 3 kV and the working distance ranged from 3 mm to 5 mm.

2.6. Tensile testing

For tensile testing, the films were cut into strips of 50 mm × 10 mm and then conditioned at 23 °C and 50 % relative humidity. An Instron 5942 Universal Testing Machine (Instron, MA, USA) was used to measure the tensile strength, strain at break, and modulus. The actual gauge length for the testing was 20 mm and a displacement rate of 2 mm/min was set as the testing parameter. At least six specimens were tested from each sample for statistical analysis. Tensile strength, strain at break, and modulus were directly provided by the Bluehill software (Instron, MA, USA). The toughness of the specimens was calculated by measuring the area under the stress-strain curve through the trapezoidal rule of area integration.

2.7. Statistical analysis

Statistical analysis was performed using IBM SPSS 28 software. An analysis of variance (ANOVA) was performed to evaluate if the shrinkage type had a statistically significant effect on density, thickness, water contact angles, oxygen and water vapor permeability, and mechanical properties. Also, Duncan's post hoc analysis was performed to classify the shrinkage types based on the group means.

3. Results and discussion

3.1. Film formation and physical properties

As stated in the introduction, the shrinkage of wet CNF films is typically restrained during drying as free drying might result in curled, wrinkled and highly roughened films. In our work, we applied a straightforward method developed through our experience to allow the radial shrinkage (xy-shrinkage) of the films while maintaining their flatness. On the other hand, for z-shrinkage, we did not apply a traditional pressure-induced restrained drying to avoid shrinkage, rather our approach was an adhesion-induced restrained drying to prepare z-films without applying any pressure from the hot press. As a result, the temperature, pressure and other processing conditions were the same for both types of films. However, the presence of filter papers on both sides of wet films in z-films can result in different evaporation rates compared to the xy-shrinkage. In brief, an 'interacting non-conforming' substrate like Whatman® filter paper is required to enable this adhesion-induced drying in z-films. The term 'interacting' refers to a material that has affinity with wet CNF mat due to the chemistry, roughness, or surface free energy, and 'non-conforming' refers to materials that do not shrink upon drying. The Whatman® filter paper used here met these two requirements.

Due to the wet film's strong adherence to the filter paper generated by the cold pressing coupled with the non-shrinking behavior of the filter paper, the shrinkage in the films was effectively restrained by adhesion to the substrate instead of applied pressure. As a result, the z-film did not have any shrinkage in the radial direction. The lack of radial shrinkage was offset by higher vertical shrinkage as listed in Table 1. The adhesion of the wet film to the filter paper, however, did not cause any macro-scale deformation or negative impact on the surface upon the removal of the filter paper except for some microscale detachment of fibrils from both surfaces, as will be detailed in Section 3.4. Films dried while attached to the filter paper are termed z-films here. On the other hand, the xy films were formed on the surface of metal plates that did not have any strong interaction with the wet mat to provide any restraint for shrinkage. As a result, xy films showed radial shrinkage while the curling of the films was prevented by the contact of the steel plates. A schematic diagram of the wet film shrinkage process of xy and z films is shown in Fig. 1b and the photographs of the dried xy and z films on top of a filter paper are shown in Fig. S1. It is important to note that after filtering the CNF suspension, a cold pressing step is essential to minimize the water content. If not adequately minimized, the higher water content can lead to rapid evaporation when it comes in contact of the hot metal plates causing immediate fracture of the films. Finally, once hot pressed and thermally compressed in the z direction, the xy- and z-films are called xy-z and z-z films, respectively.

The density of the films greatly varied depending on the type of shrinkage. As shown in Fig. 2a, xy films had a 6.8 % lower density than the z film (1.03 ± 0.04 g/cm^3). The reduced density obtained by xy-shrinkage can be explained by the synergistic effect of radial shrinkage and vertical shrinkage. The xy films shrank by 11 % in the radial direction, whereas z-films did not experience any radial shrinkage. However, both xy films and z films shrank by 45 % and 60 % in the vertical direction, respectively. The higher shrinkage in z films resulted in 27 % less thickness than the xy films, which ultimately contributed to the superior compaction and density of z films. On the other hand, thermal compression on dry xy and z films generated further vertical shrinkage. As a result, xy-z films were 12 % thinner than xy films, and z-z films were 7 % thinner than z films. The influence of thermal compression is stronger on the xy films indicating that they included more vertically oriented free space. Eventually, thermal compression converged the density of xy and z films into the same average density value (1.06 g/cm^3), suggesting that the films in this investigation were compacted to their utmost extent.

3.2. Mechanical properties

In several previous studies, CNF films were intended for high-strength and low-density applications to compete with aluminum alloys and current packaging materials; therefore, understanding their mechanical performance in terms of shrinkage type is critical (El Awad Azrak et al., 2019; Yang et al., 2020). While high strength and stiffness are desired for structural applications, packaging applications demand high flexibility, and plasticizers are typically added to improve the flexibility of CNF films at the expense of their barrier performance (Sirviö et al., 2018; Xu et al., 2019). All tensile properties studied here

Table 1
Porosity, shrinkage percentage in radial (xy) and vertical (z) direction of films with xy-shrinkage, z-shrinkage, and thermally compressed ones (xy-z, z-z).

Film type	Porosity (%)	xy-Shrinkage (%)	z-Shrinkage (%)
xy	36.1 (6.5)	11 (2.3)[a]	45.2 (7.4)
z	31.1 (8.6)	0	59.8 (1.5)
xy-z	29.6 (11.3)	11 (2.3)[b]	52.3 (3.5)
z-z	29.2 (6.3)	0	62.5 (1.5)

[a] The values in parentheses indicate the coefficient of variation (CV%).
[b] There is no further radial shrinkage upon thermal compression.

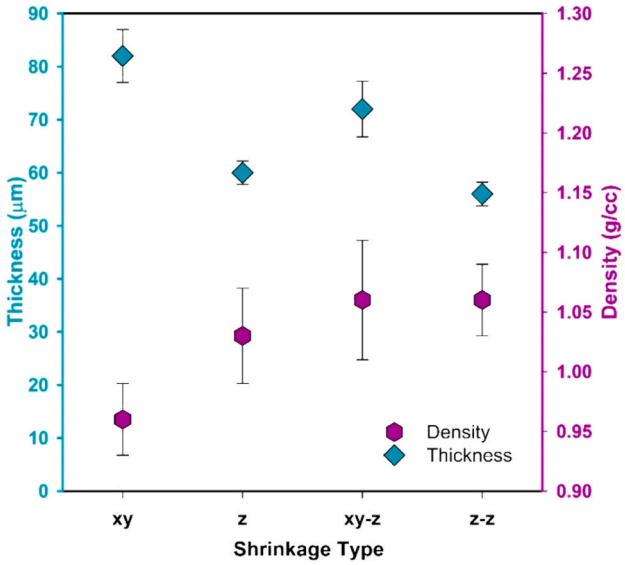

Fig. 2. Thickness and density changes for all types of shrinkage.

(listed in Table S1 and presented in Fig. 3) - tensile strength, modulus, strain at break, and toughness - showed statistically significant differences due to the shrinkage type.

The strength and modulus of z films were 35 % and 53 % greater than those of the xy films, respectively. In contrast, the xy films had 140 % and 91 % higher strain and toughness than those of z films, suggesting that the radial shrinkage gives more elongation and tougher films at the expense of reduced strength and stiffness, whereas the vertical shrinkage had the reverse effect. However, this conflict between strength and toughness is not unusual and is considered mutually exclusive for the majority of natural and manufactured materials (Ritchie, 2011). Toughness requires the capacity to dissipate local high stresses between fiber-fiber bonding by withstanding deformation, which renders hard materials brittle and lower strength materials tougher. Special engineering designs are required to make new materials with high strength and toughness (Zhu et al., 2015). Interestingly, our thermal compression technique, which further induced the z-shrinkage, improved the strength, modulus, and toughness by 12 %, 11 %, and 34 % than the non-compressed films, i.e., xy and z films. Therefore, free space reduction in vertical direction is one of the few strategies to improve the stiffness and toughness simultaneously. The relationship between the structure and mechanical properties of these films has been discussed in Section 3.4.

As previous reports (Amini et al., 2020; El Awad Azrak et al., 2019) suggest that the mechanical properties of CNF films are a function of density, we normalized the tensile strength, strain, modulus, and toughness by density and ran the statistical analysis again. After density

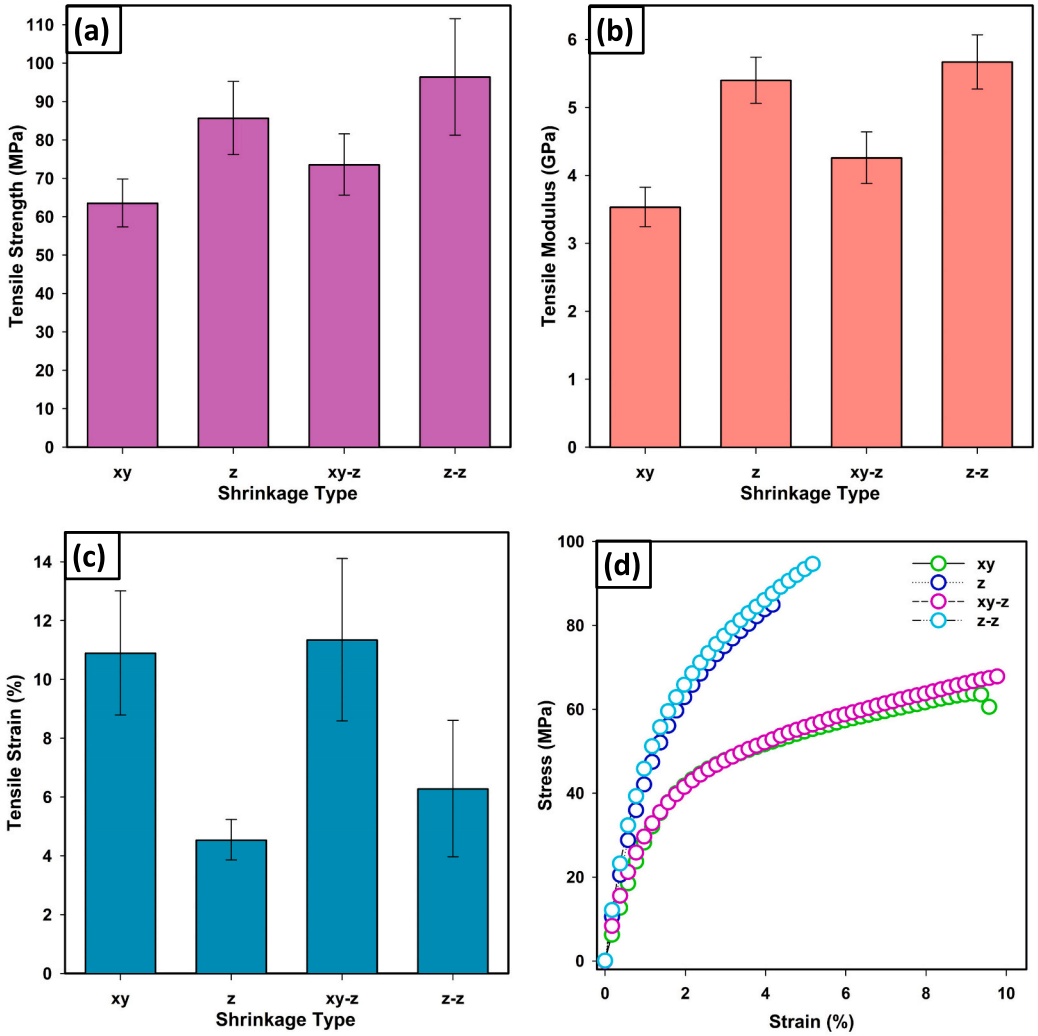

Fig. 3. Tensile strength (a), modulus (b), strain at break (c), and representative stress-strain curves (d) of xy, z, xy-z, and z-z films.

normalization, tensile strength, strain, modulus, and toughness showed statistically significant differences between the shrinkage types. Therefore, the changes observed in tensile properties could not have been solely driven by the density, but rather directly controlled by the shrinkage type. On the other hand, strength and toughness showed statistically significant differences when the thermal compression technique was applied or when it was not; however, upon density normalization, these differences became insignificant indicating that thermal compression controlled the strength and toughness by controlling the density of the films. To assess the relationship between tensile properties and thickness, four plots of strength, modulus, strain at break, and toughness against thickness were drawn (Fig. S2a–d). Interestingly, tensile strength and modulus showed a strong correlation with thickness as demonstrated by the R^2 value of 0.968 and 0.996 from the linear plot, respectively, suggesting that the strength and modulus are governed by the z-shrinkage of CNF films. On the other hand, the plots of strain-thickness and toughness-thickness showed a poor correlation with the R^2 value of 0.736 and 0.389, respectively, indicating that the strain and toughness are more likely controlled by the radial shrinkage. This observation can be very significant to tune the mechanical properties of CNF films for target applications.

3.3. Oxygen and moisture barrier performance

An excellent oxygen barrier performance at low relative humidity is one of the distinctive characteristics that made CNF films a competitive alternative to petroleum-based packaging. However, they gradually lose this property at high relative humidity (usually >65 %) as the CNF films tend to absorb moisture due to their hydrophilic structure, which can cause swelling of the fibrils and work as a medium for high gas diffusion (Paajanen et al., 2022; Wang et al., 2018). In general, the gas barrier performance of a polymeric film depends on multiple factors including the diffusivity of the gas molecules, the crystallinity of the polymer, the size of the gas molecules, the morphology of the nanoparticles in the film, and the free volume in the film (Nuruddin et al., 2021). In addition to these parameters, the water vapor permeability of hydrophilic polymeric films like CNFs is largely dependent on the strong interaction between water molecules and polymer structure (Bertuzzi et al., 2007). As a result, CNF films have high moisture transmission rate and are considered poor moisture barrier materials, although their water barrier performance is superior to paper and some other synthetic hydrophilic polymers like polyvinyl alcohol (Wang et al., 2018).

The oxygen transmission rate of xy films (Fig. 4a) was 18 % lower than that of z films, suggesting that radial shrinkage improved the oxygen barrier performance. However, this enhanced barrier performance of xy films was due to their increased thickness. As a result, the thickness normalized quantity- OP of xy films was 8 % higher than that of z films. The poor barrier performance of xy films can be attributed to the relatively porous structure induced by the radial shrinkage as listed in Table 1. Intriguingly, the difference in OP values between xy and z films became statistically insignificant upon the thermal compression. The convergence of density and porosity to a similar value upon thermal compression can be related to these similar values of xy-z and z-z films. The thermal compression technique was also reported to converge oxygen permeability values of films produced by different drying methods in our previous work (Hasan et al., 2021) and can be considered as a tool for defect removal originating from the drying process. To fully understand the underlying factors controlling the oxygen barrier performance, we studied the correlation of OTR and OP with density and thickness. However, the only good correlation identified was between OP and density with an R^2 value of 0.89 (Fig. S3a) determined from linear regression, demonstrating that oxygen permeability is highly correlated with the density of the films.

Consistent with OTR, the WVTR of xy films was likewise lower (by 9 %) than that of z films, suggesting that z films possessed a relatively poor moisture barrier, which again flipped in terms of WVP. Due to their more compact and less porous structure, the WVP of z films was 18 % less than the xy films. However, unlike OP values, WVP did not converge to a similar value upon thermal compression, albeit any correlation between OP and WVP was not necessarily expected. After thermal compression, the z-z films had 24 % less WVP than the xy-z films, indicating that the vertical shrinkage was more crucial for the water vapor barrier performance. In addition, the correlation of WVTR and WVP with density and thickness was analyzed through linear models. However, the only good correlation was observed between the WVP and thickness with an R^2 value of 0.92 from the linear plot in Fig. S3b, demonstrating that the WVP is highly correlated with thickness, rather than density.

3.4. Films' structure-property relationship

A comprehensive understanding of the film's structure is important to build a clear structure-property relationship. Fig. 5a–i shows the

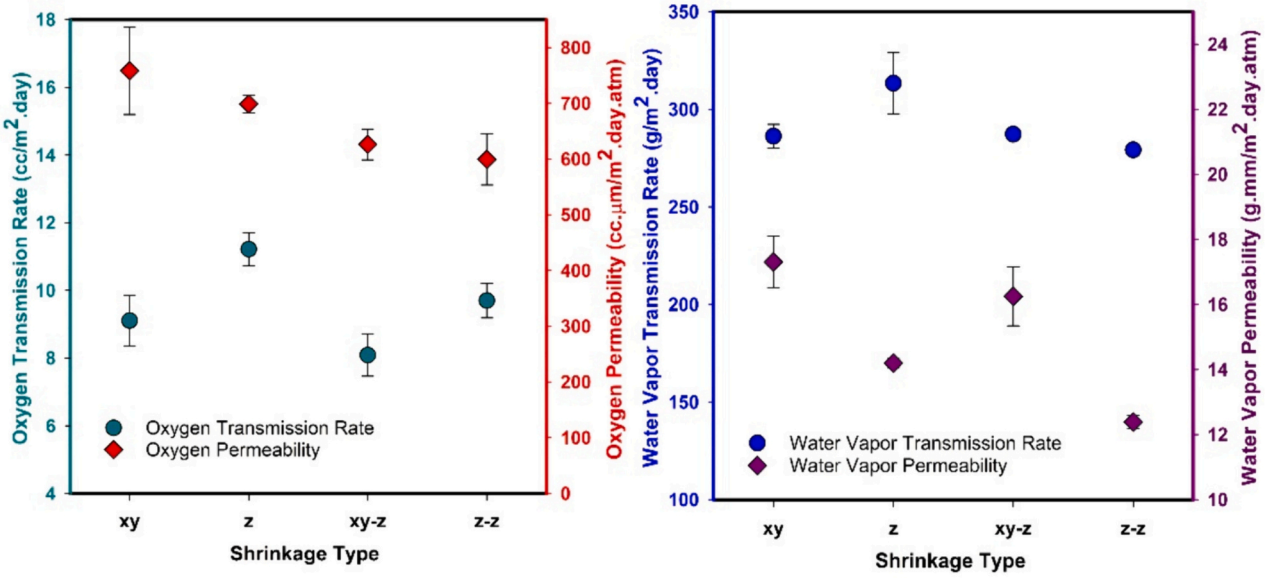

Fig. 4. Oxygen barrier performance (a) was measured at 23 °C and 80 % relative humidity, and water vapor barrier performance (b) was measured at the same temperature and 100 %/50 % relative humidity difference of various shrinkage-induced films in this study.

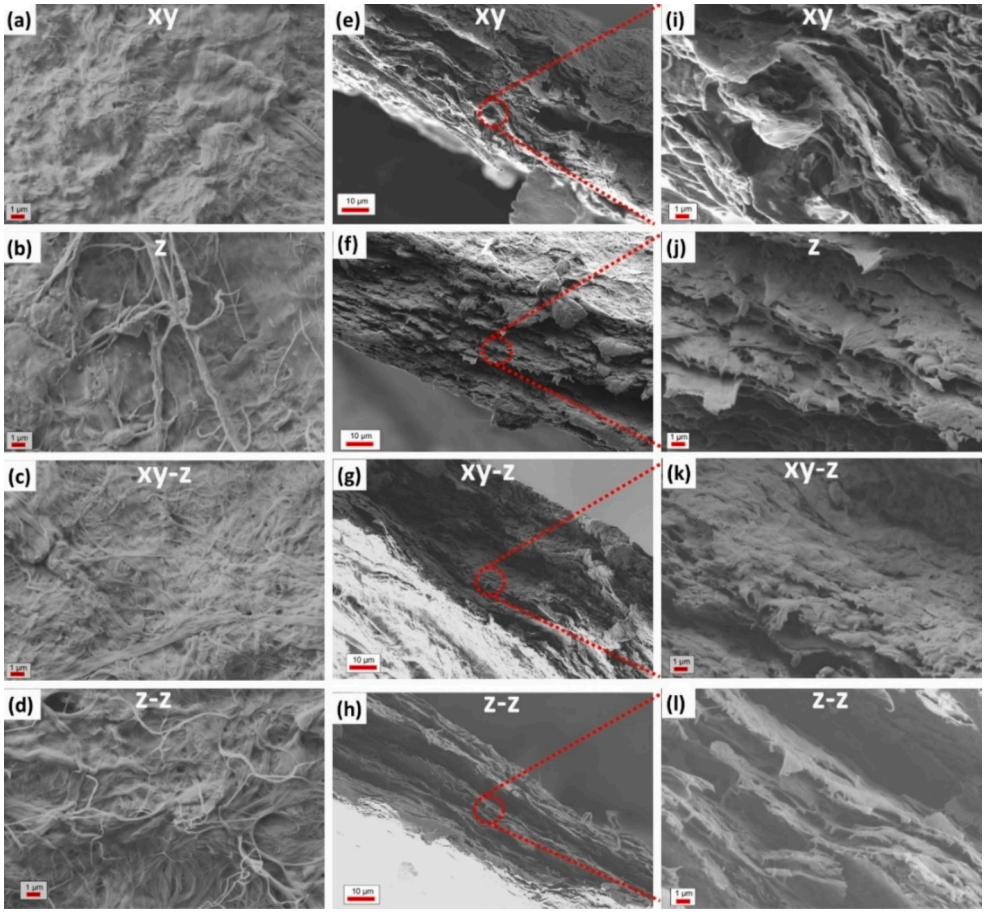

Fig. 5. SEM images of the surfaces (a–d) of xy, z, xy-z, z-z films at a magnification level of 5000× and the freeze fractured cross-sections at a magnification level of 1000× (e–h) and 5000× (i–l); the surfaces are the top surface during the filtration.

microstructure of the surfaces and freeze-fractured cross-sections of all the samples. At magnifications of 5000× (Fig. 5a–d) and 10,000× (Fig. S4e–h) on the surface images of all CNF films, the characteristic multiscale fibrous and porous structures were evident. The surface SEM images also revealed the random in-plane orientation of the fibrils as CNFs with their complex multiscale fibrillated structure prefer to form a randomly distributed wet mat from the liquid suspension and require special treatments to get orientation and anisotropic properties (Li et al., 2021). As illustrated in Fig. 5b, the most differentiating surface feature between radial and vertical shrinkage was the microlevel loose fibrillar architecture on the surfaces of z films. These hanging fibrils were relatively integrated onto the surface upon thermal compression as shown in Fig. 5d. Low magnification images (Fig. S4b, d) of their surfaces revealed that these hanging fibrils persisted all over the surfaces of the films and likely originated from the strong contact and interaction between the surfaces of wet CNF films and hydrophilic cellulose filter papers as detailed in our prior work (Hasan et al., 2021). However, the influence of these fibrils on the final macrolevel properties was not likely

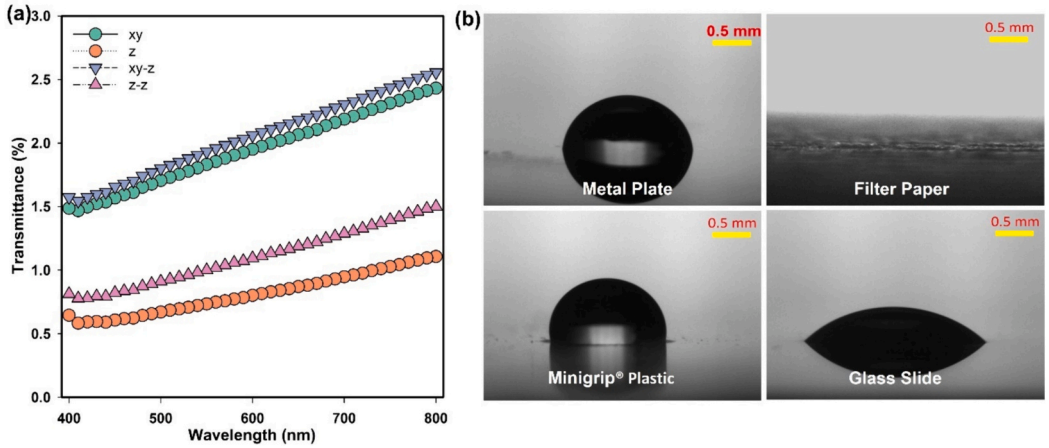

Fig. 6. (a) the transmittance of all the prepared films; (b) representative water drops on the metal plate used for the hot press, filter paper, Minigrip® plastic used instead of metal plate, and glass slide.

significant, except for the transmittance of the films. Due to the thinner and denser structure of z films than the xy films, they were expected to have better transmittance of visible lights. However, they showed an opposite trend as depicted in Fig. 6a, which can be related to the scattering of the light from those hanging fibrils of z and z-z films (Nogi et al., 2009). Moreover, the surface SEM images of xy and xy-z films indicated an uneven and dimpled surface architecture. However, it was difficult to make such comments on z and z-z films because of the presence and interference of those hanging fibrils.

The layered structure of the cross-sections of all the films has been shown in Fig. 5e–l. While the reason for the formation of such a multilayer structure is not yet fully understood, the lamellar structure of neat CNF films and their composites were reported by numerous researchers (Henriksson et al., 2008; Svagan et al., 2007). Fein et al. (2021) first proposed a skin-core model for the formation of CNF films (Fein et al., 2021). According to this model, a skin layer is formed early in the drying process of CNF films that can even create some grease barrier performance in the wet state and becomes a tightly closed surface upon drying; whereas the porosity of the films was mostly controlled by the porosity in the core structure. Comparing Fig. 5a–d & i–l, the core structure was more porous than the skin at similar magnification. Although the porosity in the core may be amplified by several folds for the defects created by the freeze-facture, it was apparent that core layers had free space among them as intra-lamellar fibrils are expected to have stronger interaction than the interlamellar fibrils. However, the combined effect of these two interactions likely controls the mechanical and barrier performance of the films. Comparing the structure of xy and z films in Fig. 5i & j, the core layers of z film were flat and straight, while the core layers of xy films were more bent and curled due to the removal of water and the action of capillary forces during drying, indicating that core layers made more space in the z direction to accommodate radial shrinkage and the deposition of bent curves on top of each other could be the potential cause of the higher porosity in xy films than the z films.

This structural feature is responsible for the difference in density and barrier performance of xy and z films. However, it cannot explain the difference in strength, modulus and strain at break of xy and z films as the curved layers became flattened in the xy-z film upon thermal compression as shown in Fig. 5k, but the difference in mechanical properties did not converge to similar values as opposed to density and oxygen permeability. Therefore, we hypothesize a "coiling" effect to be responsible for the lower mechanical properties of the xy films. CNFs are long and flexible fibers that are capable of bending and coiling during in-plane shrinkage in the xy films when fibrils are free to move unrestricted. During the tensile test, these fibrils can uncoil and straighten leading to larger strain values and lower modulus, which translate into higher toughness as, reported above. In contrast, the fibrils in z films are less coiled as they are restricted by the attachment to filter papers during drying. This leads to higher stiffness and lower strain values resulting in lower toughness for z films when compared with xy films. The subsequent thermal compression step is unable to uncoil the coiled fibrils as they exist in the xy plane and that is why the difference between the mechanical properties of the two shrinkage type films persists upon densification.

The evolution of the intra-lamellar fibrils' interaction from wet state to dry state by radial and vertical shrinkage was difficult to track with SEM. We utilized a simple polarized light microscope to observe the shrinkage during drying. However, it was equally challenging to track the fibrils of a vacuum filtered film through an optical microscope due to the high thickness of the films, curling, as well as blockage of light caused by the filter paper to track z films. As a result, we were motivated to track a drop cast solution on a transparent surface with equivalent surface properties of the metal plate (xy film) and filter paper. Measuring the water contact angle of filter papers was tough as they absorb the water immediately after dropping (<1 s), but indicated a very hydrophilic surface. Microscope glass slides also showed a very low water contact angle (40°), a close representation of the filter paper. On the other hand, the Minigrip® plastic (a regular re-closable bag used in the lab and mostly low-density polyethylene) showed an average water contact angle of 99°, which was also close to the water contact angle of the metal plate (83°). A representative water droplet on all the surfaces has been shown in Fig. 6b.

Fig. 7a–h shows how the dry line (edge of the droplet) on a plastic surface (Fig. 7a–d) and glass surface (Fig. 7e–h) proceeded with time. A full droplet drying pattern on both surfaces is also available in Fig. S5a–f. The drying of a single droplet of very low volume (~0.5 mL) and low solids content is likely to give some insights into the single layer formation process of casted CNF films. Although the drop casting process ignored the fact that the film structure was already established during the filtration and before the drying, this simple method still helped understand the influence of drying substrates (interacting or non-interacting) on shrinkage. It is evident from Fig. 7a–d that the contact line of the droplet on the plastic surface was not pinned, rather it moved towards the center of the droplet with the increase in solid content due to the hydrophobicity of the surface. The movement of the droplet towards the center also pushed the fibrils towards the center as the fibrils did not have any affinity with the surface and they had a strong cohesive force with themselves and water molecules. However, to accommodate the extra fibrils in a relatively smaller area, the fibrils tend to arrange in the z-direction as well. This z-directional arrangement during drying on a non-interacting surface might cause the thickness and roughness increase of each layer in the lamellar structure. This can be further proved by the fact that xy-z films had greater thickness than the z-z films although they had similar porosity, and both underwent the thermal compression process. The SEM images of cross-sections (Fig. 5k, l) also seemed to exhibit a rougher surface for xy-z films. This higher thickness of the individual layer likely caused the difference in the mechanical performance of xy and z films as well. However, further study is required to establish the relationship between the thickness of the individual layers and the final properties of the films.

In contrast, the droplet on the glass slide was pinned on the surface due to the hydrophilic nature of the glass slide and the contact line did not show any movement during the whole drying process. The micron-level fibrils had very little amount of random movement during the drying process (not shown in the picture). As a result, larger fibrils stayed almost at the same position they were initially cast. However, tiny circular particles had a motion in the radial direction. As the droplet was pinned and the particle size was circular, they slightly formed so-called 'coffee ring' structure at the dry line (Yunker et al., 2011). On the other hand, a drying line also proceeded from the initial dry line to the center of the droplet at the last stage of drying, which was not visible for the droplets on the plastic surface. Moreover, fibrils were not forced to arrange in the z-direction, so each layer in the lamellar structure could be smooth and thinner than the xy films, which eventually led to a lower thickness of the overall film and contributed to enhanced strength and stiffness, as well as barrier performance. During the actual filtration process, CNFs are most likely to sequentially deposit on the previously deposited layer. In reality, the entangled particles conform to and are constrained by the previous layer. Individual layers are locked by the top and bottom layers and thus the film cannot shrink on the filter paper. On the other hand, the whole film has the freedom to shrink together on the steel surfaces, albeit interlayer movement may not be pronounced. Through this section, we tried to highlight the film and single layer formation strategy based on different shrinkage types and relate it to the properties. However, the CNF film formation strategy is not fully understood, especially how individual fibril morphology changes in response to different drying conditions. For example, individual fibrils may coil up in unrestrained drying condition and uncoil upon tensile testing. A detailed separate study would be required to completely understand this phenomenon.

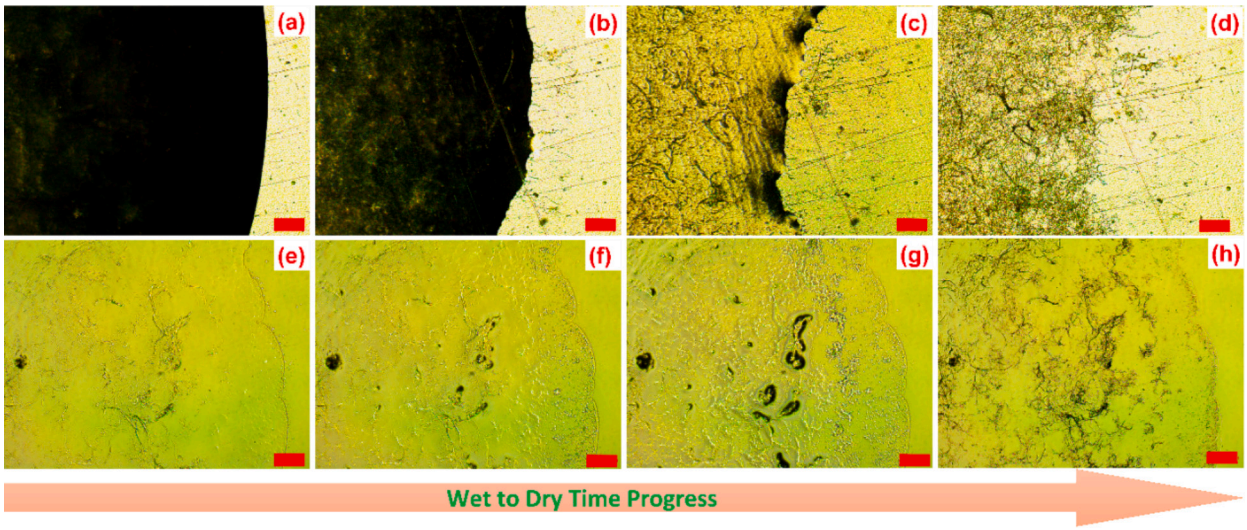

Fig. 7. The time progress of the edge of a CNF solution droplet from a wet state to a dry state on a Minigrip® plastic surface (a–d) and a glass slide (d–f); the scale bar indicates 200 μm.

4. Conclusions

In this study, we have shown that depending on the shrinkage mode, the morphology, mechanical and barrier properties of CNF films can be significantly different. Based on the results and discussions provided above, we conclude that our hypothesis that the shrinkage of CNF films during drying process is one of the major factors that can significantly influence physical, mechanical and barrier properties of CNF films, can be confirmed. We also highlight the need for mentioning the shrinkage percentage in radial and vertical direction to be able to correctly compare between different studies, even though the sources CNF suspension and other preparation parameters are same. The xy film studied here had 11 % radial shrinkage and 45 % vertical shrinkage whereas the z film had no radial shrinkage and 60 % vertical shrinkage. The radial shrinkage in xy films resulted in a more porous structure due to the curved structure of individual layers in the core structure of the films as revealed by the SEM images. As a result of higher porosity, the xy films had higher oxygen permeability than the z films. However, thermal compression on dry xy and z films resulted in the same density and oxygen permeability value as oxygen permeability was found to be correlated with density, while the water vapor permeability was found to be correlated with z-shrinkage. The radial shrinkage brought about a more extensible and tougher film, whereas vertical shrinkage tended to result in a strong and stiff film attributed to a possible coiling effect upon drying and in-plane shrinkage. Due to the interaction between wet film and filter paper, z films had loosely hanging fibrils on their surface that increased the light scattering from the surface. A single layer formation of a drop cast film on a hydrophilic and hydrophobic surface suggested that radial shrinkage is likely to form a thicker individual layer in the core structure and the opposite for the vertical shrinkage. A coffee ring effect was seen for the droplet on the glass surface. This research sheds light on the shrinkage of CNF films, which has been generally ignored to relate to the final mechanical and barrier properties. Future research direction in this area will be on how to control the amount of shrinkage and a detailed study on the drop cast drying patterns for all the different kinds of cellulose nanomaterials to understand their self-assembly in a better way.

CRediT authorship contribution statement

Md Ikramul Hasan: Writing – review & editing, Writing – original draft, Validation, Methodology, Investigation, Formal analysis, Data curation, Conceptualization. **Jinwu Wang:** Writing – review & editing, Supervision, Resources, Project administration, Methodology, Investigation, Conceptualization. **Mehdi Tajvidi:** Writing – review & editing, Resources, Project administration, Methodology, Funding acquisition, Formal analysis, Conceptualization.

Declaration of competing interest

The authors declare that they have no known competing financial interests or personal relationships that could have appeared to influence the work reported in this paper.

Data availability

Data will be made available on request.

Acknowledgements

The authors would like to thank Dr. Emma Perry for helping with the Scanning Electron Microscopy. This work was partially supported through the agreement 19-JV-11111124-062 between the U.S. Forest Service and the University of Maine, UMaine Paper Surface Science Program (PSSP). This project was also supported by the USDA National Institute of Food and Agriculture, McIntire-Stennis, Project #042120.

Appendix A. Supplementary data

Supplementary data to this article can be found online at https://doi.org/10.1016/j.carbpol.2024.122390.

References

Abdul Khalil, H. P. S., Bhat, A. H., & Ireana Yusra, A. F. (2012). Green composites from sustainable cellulose nanofibrils: A review. *Carbohydrate Polymers, 87*(2), 963–979. https://doi.org/10.1016/j.carbpol.2011.08.078

Amini, E., Hafez, I., Tajvidi, M., & Bousfield, D. W. (2020). Cellulose and lignocellulose nanofibril suspensions and films: A comparison. *Carbohydrate Polymers, 250*(August), Article 117011. https://doi.org/10.1016/j.carbpol.2020.117011

Barlow, C. Y., & Morgan, D. C. (2013). Polymer film packaging for food: An environmental assessment. *Resources, Conservation and Recycling, 78*, 74–80. https://doi.org/10.1016/j.resconrec.2013.07.003

Bertuzzi, M. A., Castro Vidaurre, E. F., Armada, M., & Gottifredi, J. C. (2007). Water vapor permeability of edible starch based films. *Journal of Food Engineering, 80*(3), 972–978. https://doi.org/10.1016/j.jfoodeng.2006.07.016

Bilodeau, M., & Paradis, M. (2018). High Efficiency Production of Nanofibrillated Cellulose, US Patent No. 9,988,762 B2. Washington, DC: US Patent and Trademark Office.

Chen, Y., Zhang, L., Yang, Y., Pang, B., Xu, W., Duan, G., … Zhang, K. (2021). Recent progress on nanocellulose aerogels: Preparation, modification, composite fabrication, applications. *Advanced Materials, 33*(11). https://doi.org/10.1002/adma.202005569

El Awad Azrak, S. M., Clarkson, C. M., Moon, R. J., Schueneman, G. T., & Youngblood, J. P. (2019). Wet-stacking lamination of multilayer mechanically fibrillated cellulose nanofibril (CNF) sheets with increased mechanical performance for use in high-strength and lightweight structural and packaging applications. *ACS Applied Polymer Materials, 1*(9), 2525–2534. https://doi.org/10.1021/acsapm.9b00635

Fein, K., Bousfield, D. W., & Gramlich, W. M. (2021). Processing effects on structure, strength, and barrier properties of refiner-produced cellulose nanofibril layers. *ACS Applied Polymer Materials, 3*(7), 3666–3678. https://doi.org/10.1021/acsapm.1c00620

Gao, H., Li, J., Zhang, F., Liu, Y., & Leng, J. (2019). The research status and challenges of shape memory polymer-based flexible electronics. *Materials Horizons, 6*(5), 931–944. https://doi.org/10.1039/C8MH01070F

Ghasemi, S., Rahimzadeh-Bajgiran, P., Tajvidi, M., & Shaler, S. M. (2020). Birefringence-based orientation mapping of cellulose nanofibrils in thin films. *Cellulose, 27*(2), 677–692. https://doi.org/10.1007/s10570-019-02821-2

Hafez, I., & Tajvidi, M. (2021). Comprehensive insight into foams made of thermomechanical pulp fibers and cellulose nanofibrils via microwave radiation. *ACS Sustainable Chemistry and Engineering, 9*(30), 10113–10122. https://doi.org/10.1021/acssuschemeng.1c01816

Hasan, I., Wang, J., & Tajvidi, M. (2021). Tuning physical, mechanical and barrier properties of cellulose nanofibril films through film drying techniques coupled with thermal compression. *Cellulose, 28*(18), 11345–11366. https://doi.org/10.1007/s10570-021-04269-9

Henriksson, M., Berglund, L. A., Isaksson, P., Lindström, T., & Nishino, T. (2008). Cellulose nanopaper structures of high toughness. *Biomacromolecules, 9*(6), 1579–1585. https://doi.org/10.1021/bm800038n

Ketola, A. E., Strand, A., Sundberg, A., Kouko, J., Oksanen, A., Salminen, K., … Retulainen, E. (2019). Effect of micro- and nanofibrillated cellulose on the drying shrinkage, extensibility, and strength of fibre networks. *BioResources, 13*(3), 5319–5342. https://doi.org/10.15376/biores.13.3.5319-5342

Kouko, J., & Retulainen, E. (2018). The relationship between shrinkage and elongation of bleached softwood kraft pulp sheets. *Nordic Pulp and Paper Research Journal, 33*(3), 522–533. https://doi.org/10.1515/npprj-2018-3057

Lerouge, T., Maillet, B., Coutier-Murias, D., Grande, D., Le Droumaguet, B., Pitois, O., & Coussot, P. (2020). Drying of a compressible biporous material. *Physical Review Applied, 13*(4), 1. https://doi.org/10.1103/PhysRevApplied.13.044061

Li, K., Clarkson, C. M., Wang, L., Liu, Y., Lamm, M., Pang, Z., … Ozcan, S. (2021). Alignment of cellulose nanofibers: Harnessing nanoscale properties to macroscale benefit. *ACS Nano, 15*(3), 3646–3673. https://doi.org/10.1021/acsnano.0c07613

Moon, R. J., Martini, A., Nairn, J., Simonsen, J., & Youngblood, J. (2011). Cellulose nanomaterials review: Structure, properties and nanocomposites. *Chemical Society Reviews, 40*(7). https://doi.org/10.1039/c0cs00108b

Nogi, M., Iwamoto, S., Nakagaito, A. N., & Yano, H. (2009). Optically transparent nanofiber paper. *Advanced Materials, 21*(16), 1595–1598. https://doi.org/10.1002/adma.200803174

Nuruddin, M., Chowdhury, R. A., Szeto, R., Howarter, J. A., Erk, K. A., Szczepanski, C. R., & Youngblood, P. (2021). Structure − property relationship of cellulose nanocrystal − polyvinyl alcohol thin films for high barrier coating applications. *ACS Applied Materials & Interfaces, 13*(10), 12472–12482. https://doi.org/10.1021/acsami.0c21525

Paajanen, A., Zitting, A., Rautkari, L., & Ketoja, J. A. (2022). *Nanoscale mechanism of moisture-induced swelling in wood microfibril bundles*. https://doi.org/10.1021/acs.nanolett.2c00822

Paquet, C., & Kumacheva, E. (2008). Nanostructured polymers for photonics. *Materials Today, 11*(4), 48–56. https://doi.org/10.1016/S1369-7021(08)70056-7

Qing, Y., Sabo, R., Wu, Y., Zhu, J. Y., & Cai, Z. (2015). Self-assembled optically transparent cellulose nanofibril films: Effect of nanofibril morphology and drying procedure. *Cellulose, 22*(2), 1091–1102. https://doi.org/10.1007/s10570-015-0563-9

Ritchie, R. O. (2011). The conflicts between strength and toughness. *Nature Materials, 10*(11), 817–822. https://doi.org/10.1038/nmat3115

Sim, K., Ryu, J., & Youn, H. J. (2015). Structural characteristics of nanofibrillated cellulose mats: Effect of preparation conditions. *Fibers and Polymers, 16*(2), 294–301. https://doi.org/10.1007/s12221-015-0294-4

Sirviö, J. A., Visanko, M., Ukkola, J., & Liimatainen, H. (2018). Effect of plasticizers on the mechanical and thermomechanical properties of cellulose-based biocomposite films. *Industrial Crops and Products, 122*, 513–521. https://doi.org/10.1016/j.indcrop.2018.06.039

Svagan, A. J., Azizi Samir, M. A. S., & Berglund, L. A. (2007). Biomimetic polysaccharide nanocomposites of high cellulose content and high toughness. *Biomacromolecules, 8*(8), 2556–2563. https://doi.org/10.1021/bm0703160

Tayeb, A. H., Amini, E., Ghasemi, S., & Tajvidi, M. (2018). Cellulose nanomaterials-binding properties and applications: A review. *Molecules, 23*(10), 1–24. https://doi.org/10.3390/molecules23102684

Wang, J., Gardner, D. J., Stark, N. M., Bousfield, D. W., Tajvidi, M., & Cai, Z. (2018). Moisture and oxygen barrier properties of cellulose nanomaterial-based films. *ACS Sustainable Chemistry and Engineering, 6*(1), 49–70. https://doi.org/10.1021/acssuschemeng.7b03523

Wu, D., Engqvist, J., Barbier, C., Karlsson, C., & Hall, S. (2022). Unravelling the deformation process of a compacted paper: In-situ tensile loading, 4D X-ray tomography and image-based analysis. *International Journal of Solids and Structures, 242*(October 2021), Article 111539. https://doi.org/10.1016/j.ijsolstr.2022.111539

Xu, J., Xia, R., Zheng, L., Yuan, T., & Sun, R. (2019). Plasticized hemicelluloses/chitosan-based edible films reinforced by cellulose nanofiber with enhanced mechanical properties. *Carbohydrate Polymers, 224*, Article 115164. https://doi.org/10.1016/j.carbpol.2019.115164

Yang, X., Reid, M. S., Olsén, P., & Berglund, L. A. (2020). Eco-friendly cellulose nanofibrils designed by nature: Effects from preserving native state. *ACS Nano, 14*(1), 724–735. https://doi.org/10.1021/acsnano.9b07659

Yunker, P. J., Still, T., Lohr, M. A., & Yodh, A. G. (2011). Suppression of the coffee-ring effect by shape-dependent capillary interactions. *Nature, 476*(7360), 308–311. https://doi.org/10.1038/nature10344

Zhu, H., Zhu, S., Jia, Z., Parvinian, S., Li, Y., Vaaland, O., Hu, L., & Li, T. (2015). Anomalous scaling law of strength and toughness of cellulose nanopaper. *Proceedings of the National Academy of Sciences of the United States of America, 112*(29), 8971–8976. https://doi.org/10.1073/pnas.1502870112